

Medical needle tip tracking based on Optical Imaging and AI

Zhuoqi Cheng^{a,*}, Simon Lyck Bjært Sørensen^a, Mikkel Werge Olsen^a, René Lyng Eriksen^b, Thiusius Rajeeth Savarimuthu^a

^a*Maersk Mc-Kinney Møller Institute, University of Southern Denmark, Odense, 5230, Denmark*

^b*Mads Clausen Institute, University of Southern Denmark, Odense, 5230, Denmark*

Abstract

Background and Objective: Deep needle insertion to a target often poses a huge challenge, requiring a combination of specialized skills, assistive technology, and extensive training. One of the frequently encountered medical scenarios demanding such expertise includes the needle insertion into a femoral vessel in the groin. After the access to the femoral vessel, various medical procedures, such as cardiac catheterization and extracorporeal membrane oxygenation (ECMO) can be performed. However, even with the aid of Ultrasound imaging, achieving successful insertion can necessitate multiple attempts due to the complexities of anatomy and tissue deformation.

Methods: To address this challenge, this paper presents an innovative technology for needle tip real-time tracking, aiming for enhanced needle insertion guidance. Specifically, our approach revolves around the creation of scattering imaging using an optical fiber-equipped needle, and uses Convolutional Neural Network (CNN) based algorithms to enable real-time estimation of the needle tip's position and orientation during insertion procedures.

Results: The efficacy of the proposed technology was rigorously evaluated through three experiments. The first two experiments involved rubber and bacon phantoms to simulate groin anatomy. The positional errors averaging 2.3 ± 1.5 mm and 2.0 ± 1.2 mm, and the orientation errors averaging 0.2 ± 0.11 rad and 0.16 ± 0.1 rad. Furthermore, the system's capabilities were validated through experiments conducted on fresh porcine phantom mimicking more complex anatomical structures, yielding positional accuracy results

*Corresponding author: zch@mmmi.sdu.dk

of 3.2 ± 3.1 mm and orientational accuracy of 0.19 ± 0.1 rad.

Conclusions: Given the average femoral arterial radius of 4 to 5 mm, the proposed system is demonstrated with a great potential for precise needle guidance in femoral artery insertion procedures. In addition, the findings highlight the broader potential applications of the system in the medical field.

Keywords: Needle tip tracking, Optical needle, Scattering imaging, Deep Learning

1. Introduction

Deep needle insertion is a medical procedure that allows medical professionals inserting a needle from the skin and reach targets located beneath the surface, such as tumors, nerves, or blood vessels. It plays a crucial role in enabling precise and targeted medical interventions such as administering medication, obtaining samples, or carrying out therapeutic procedures. Therefore, deep needle insertion is widely utilized across a diverse range of medical disciplines, including deep vessel interventions, biopsies, brachytherapy, interventional radiology, anesthesia, and pain management.

Despite its wide applications, deep needle insertion presents inherent challenges and requires both expertise and technological support [1]. One of the main difficulties encountered in this procedure is the deformation of soft tissue during insertion. As the needle penetrates the body, the surrounding tissues have a tendency to move, making it challenging to precisely reach the intended target. Moreover, once the needle tip is within the tissue, its visibility becomes obscured, complicating the accurate tracking of its exact location. This lack of visibility becomes particularly problematic when encountering resistant tissues, as it frequently results in needle deflection, further impeding the ability to precisely locate the needle.

Frequently, healthcare professionals rely on imaging techniques to guide needle insertion, with ultrasound (US) and fluoroscopy being commonly used modalities [2, 3, 4]. These imaging technologies provide real-time visualization of the needle and surrounding anatomical structures, aiding in the precise localization of the target and facilitating adjustments to the insertion direction. However, the effectiveness of using this technique heavily depends on the practitioner's experience and necessitates extensive training to ensure proficiency [5]. Advancements in robotics for needle deep insertion have

been explored in the literature [6]. A typical exploitation of robotic and artificial intelligence (AI) technology is through the extraction and detection of the needle tip from US images [7]. Nevertheless, given the inherent noise in US imaging, the utilization of complex image processing algorithms and substantial computing power is required [8].

In addition to the previously described image-guided needle insertion method, needle guidance technology can also incorporate embedded sensors, particularly for the task of needle tip tracking (NTT). Previous studies have explored the use of concentric electrode needle for electrical bioimpedance sensing [9]. But the functionality of this technology is to detect the type of tissue in contact with the needle, rather than to provide the spatial position of the needle tip [10]. Alternatively, other studies have utilized electromagnetic (EM) sensors embedded in needle tips to enable tracking within a generated magnetic field [11]. Research indicates that in favorable environments, an average accuracy of 1 mm can be achieved [12]. However, the use of EM sensors presents several challenges. Firstly, calibration is required for seamless integration into the workflow. Secondly, the tracking accuracy is contingent on the absence of metal and magnetic fields in the environment. Lastly, the implementation of EM sensors can be relatively costly.

Alternatively, the NTT can be achieved by leveraging the accurate model of the needle deflection. Shape sensing techniques, such as strain gauges and Fiber Bragg Gratings (FBG), can be attached along the needle shaft to retrieve information on the needle’s deflection [13]. However, the FBG technology, while offering accurate needle shape reconstruction in real-time, is sensitive to temperature variations and can be relatively expensive to implement.

The objective of this study is to present a novel sensing method for tracking the position of a needle tip accurately and in real time. As shown in Figure 1(A), the proposed method incorporates an optical fiber within the lumen of the needle to emit light at the needle tip. By capturing the light scattering imaging on the tissue surface, an AI-empowered image processing algorithm is employed to analyze the images and estimates the spatial position of the needle tip. The primary focus of this research is to utilize this technique for guiding needle insertion into deep vessels in the groin region, with the ultimate aim of enhancing patient care through improved effectiveness and efficiency. To the best of the authors’ knowledge, the proposed NTT approach presents a pioneering advancement, and holds significant potential for extension to various other applications such as vessel puncture detection.

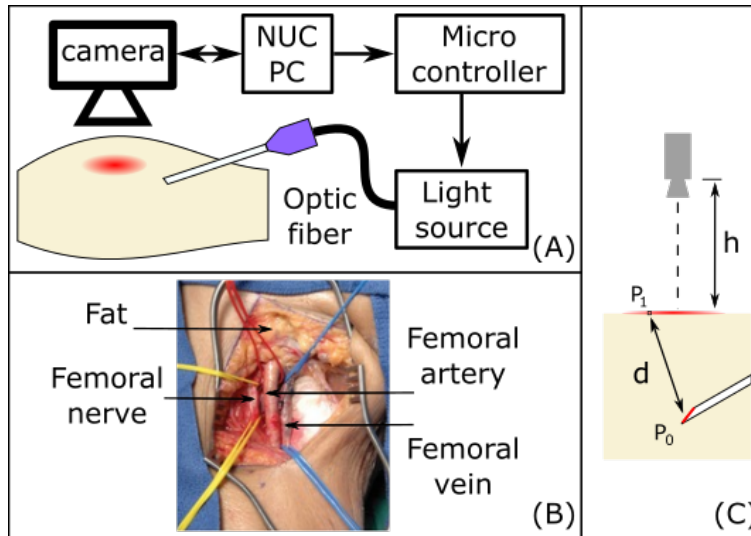


Figure 1: (A) The proposed system configuration includes a camera, a PC, a micro-controller, a light source and a needle with embedded optic fiber; (B) The anatomy of groin area where a femoral artery is covered under skin and a layer of fat; (C) The modeling of optic imaging generated by lighting at the needle tip.

2. Material and methods

2.1. Design concept and requirements

As described, one of the primary applications for the proposed technology is to facilitate the guidance of needle insertion into the femoral artery in the groin area. As illustrated in Figure 2(B), the artery is ensconced within layers of adipose tissue and connective tissue beneath the skin. The distance between the skin surface and the femoral artery in the groin area is subject to variation, particularly in relation to the patient's body mass index (BMI). In individuals of normal weight for their height, the femoral artery usually resides 2 to 3 cm below the skin. For those with obesity, the artery can be positioned as deep as 4 cm [14, 15].

Figure 1(C) shows a simplified model that treats the skin and adipose tissues together as a homogeneous material, assuming a uniform optical property for both [16]. Given that the bevel tip of the needle consistently points upward during insertion, once the needle tip penetrates the tissue, the light emitted from it travels through the tissue and generates a scattering image on the skin's surface. Moreover, we assume that the tissue surface is flat.

The Bouguer-Beer-Lambert law, an exponential function, governs the intensity of the light as it travels through the tissue, causing it to attenuate. We further denote the light intensity emitting from the needle tip as I_0 . In this case, the intensity at point P_1 can be calculated as follows:

$$I(P_1) = (1 - R_F)I_0 \exp(-\mu_t d) \quad (1)$$

where d is the distance between the light source P_0 and P_1 , R_F and μ_t represent the diffuse Fresnel reflectance and the attenuation coefficient of tissue respectively.

In addition, the current system set the distance between the tissue surface and the camera’s imaging plane, h , as a fixed value. According to Equation 1, the generated scattering imaging on the tissue surface has a unique mapping to the needle tip relative position inside the tissue. Since establishing the correlation between the needle tip position and the produced scattering image is complex, an AI based method is developed in this study.

2.2. System setup

Figure 2 depicts the system setup based on the proposed concept. The system incorporates a custom-designed needle (shown in Figure 2(B)) which is created by inserting an optic fiber (M137L02, Thorlabs Inc., US) into the lumen of a 22G needle and then securing the two components with glue. The Thorlabs 880 nm LED is selected as the light source, because the near-infrared (NIR) spectrum has a relatively lower absorption rate in tissue compared to visible light, enabling the light to penetrate thicker tissue [16]. Additionally, the selected light source has a power output of about 0.6 mW, which provides sufficient intensity while maintaining safety.

The control and data acquisition system is based on a portable PC (NUC10i7), which manages a micro-controller (Arduino UNO) for toggling the light source on and off. In addition, a camera (ASI178MM, ZWO Co. Ltd., China) is positioned 100 mm above the tissue surface and interfaced with the PC to capture the scattering image.

This study also employs a TrakSTAR electromagnet (EM) tracking system (NDI Inc., Canada) to track the spatial position of the needle tip, serving as the ground-truth values for supervised learning. The EM sensor system comprises two main components: a coil and an EM sensor. The coil is securely fastened onto the platform, while the EM sensor is affixed to the needle hub. Please note that the EM sensor is only used for acquiring needle tip

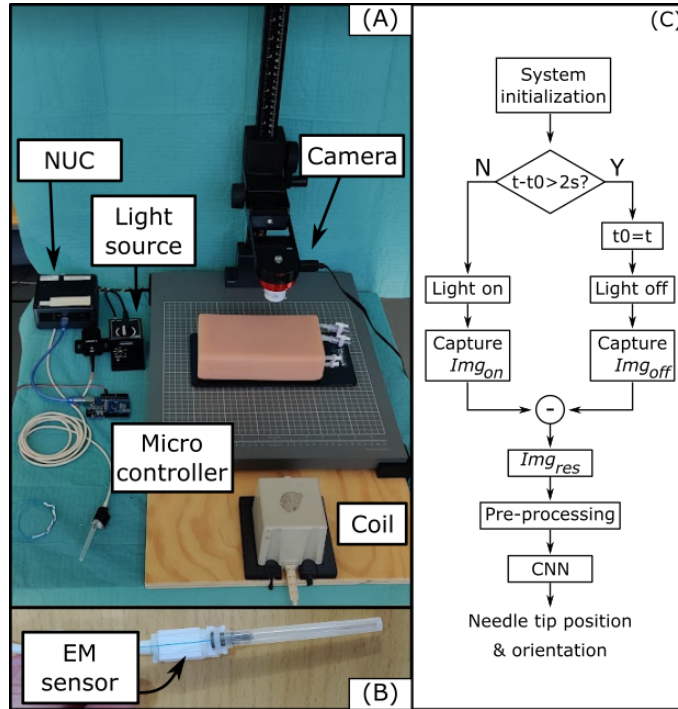


Figure 2: (A) The system setup for validating the proposed concept, (B) The EM sensor is fixed to the needle hub for obtaining the ground-truth position & orientation values, and (C) The workflow of the software system.

position to feed the network training, and is not necessary for the actual deployment.

For data collection, the software system is constructed using the Robot Operation System (ROS) framework, which operates on the NUC PC. Additionally, a system with a Threadripper 5965WX CPU and an NVIDIA RTX 6000 Ada Generation GPU is used for training the AI algorithm which is developed based on PyTorch [17] with PyTorch Lightning [18]. After the AI model has been fully trained, it is tested on the NUC PC to assess its efficacy and performance. We choose to implement the final system on the NUC PC for consideration of system portability.

2.3. Calibration

The calibration procedure comprises two essential steps.

Firstly, the intrinsic parameters of the camera should be acquired in order to generate a distortion-free imaging. This is done by utilizing a chessboard

pattern to ensure accurate mapping between real-world coordinates and their corresponding image coordinates. OpenCV lib is employed for calculating these required camera parameters.

Secondly, a coordinate transformation is performed to establish a mapping between the coordinate of the needle tip $\{N\}$ in relation to the global coordinate on the platform $\{G\}$. This task is accomplished through the EM sensor, whose relative position in relation to the coil \mathbf{T}_{EM}^{Coil} can be obtained directly. As shown in Figure 3, a pivot calibration is done by manually controlling the needle tip to the origin of $\{G\}$ multiple times and at varying orientations. By collecting a series of data, we can retrieve the relation between the EM sensor and the needle tip, namely \mathbf{T}_N^{EM} . Subsequently, the needle tip is navigated to 9 predefined points on the platform, arranged in 3 rows and 3 columns and spaced 30 mm apart. The center of these 9 points is the origin of $\{G\}$. The least square method is used to fit the collected points, and we can calculate the transformation matrix between the coil frame and the global frame as \mathbf{T}_{Coil}^G . The parameter fitting procedure also calculate the residual which corresponds to the Euclidean distance reprojection error of 0.64 mm. With the above transformation matrix obtained, the position of the needle tip in the global coordinate system can be calculated as follows:

$$\mathbf{T}_N^G = \mathbf{T}_{Coil}^G \cdot \mathbf{T}_{EM}^{Coil} \cdot \mathbf{T}_N^{EM} \quad (2)$$

2.4. Data acquisition

To acquire the required data for training and validating the proposed system, a software system is designed following the workflow illustrated in Figure 2(C). This system runs in a loop, and controls the activation and deactivation of the light source during data acquisition process. Images are taken with the needle light on (Img_{on}) continuously only interrupted by an ambient light image (Img_{off}) taken every 2s with the needle light off. With the use of the newest ambient light image, each illuminated image ambient light can be removed with $Img_{res} = Img_{on} - Img_{off}$ (see Figure 4). The residual image Img_{res} is then published to the *ROS* network.

During the data acquisition, the user press a button on the keyboard and the system automatically save the residual image (down-scaled to 400×400) and the current needle tip position with respect to the global coordinate.

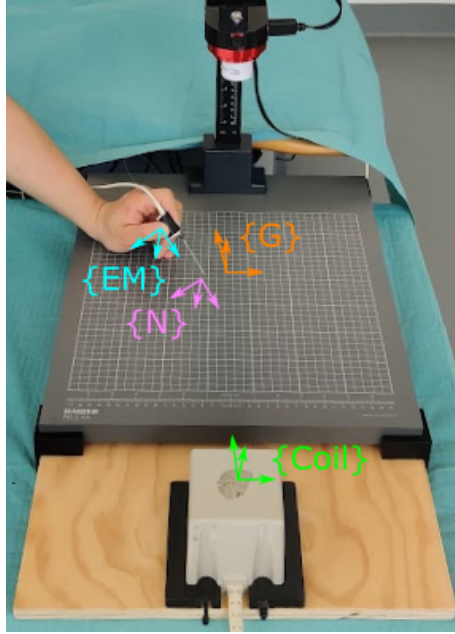


Figure 3: Reference frames of the system: $\{G\}$ global frame, $\{N\}$ needle tip frame, $\{EM\}$ EM sensor frame, and $\{Coil\}$ coil frame.

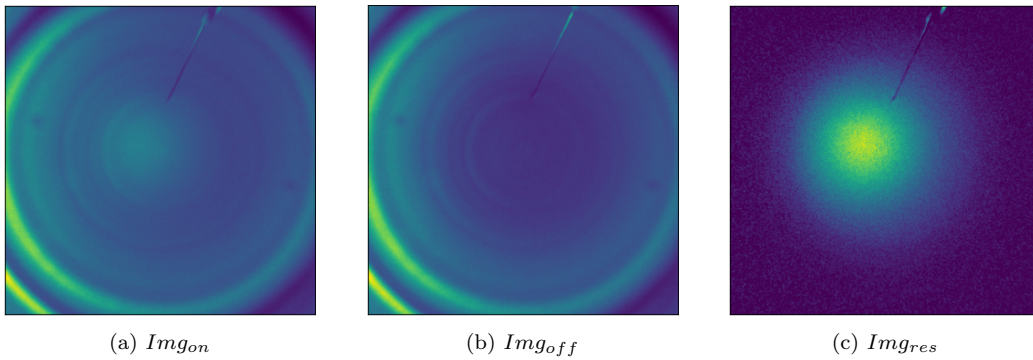


Figure 4: Through activating and deactivating the light source, the influence of ambient light can be removed, and the residual imaging $Img_{on} - Img_{off} = Img_{res}$ can be obtained.

2.5. Data normalization

In the context of neural networks receiving images as input, each image is divided by the maximum pixel value to enhance convergence for the model. The images are initially stored in a uint16 format, with a pixel value range spanning from 0 to 65535. Consequently, the images are normalized to a range of $[0, 1]$.

Moreover, the 3D positional information corresponds to a spatial region within the global coordinate system. To ensure consistent data representation, the positional data in the X and Y axes are further normalized to the range of $[-1, 1]$, while the Z-axis data is normalized to the range of $[0, 1]$.

2.6. Quaternion processing

Quaternion is used in this study to represent orientation of the needle tip. Due to the unit norm constraint, the direct probabilistic modeling of quaternion trajectories becomes intractable. For this, we use the method for converting quaternion into Euclidean space presented in [19]. An auxiliary quaternion q_0 is introduced, and a 4-D quaternion q_1 can be transformed to a 3-D vector ζ by calculating the logarithm of orientation difference as follows:

$$\zeta(q_1) = \log(q_1 * q_0) = \begin{cases} \arccos v \frac{\mathbf{u}}{\|\mathbf{u}\|} & \text{if } \mathbf{u} \neq 0 \\ [0 \ 0 \ 0]^T & \text{if } otherwise. \end{cases} \quad (3)$$

where v and \mathbf{u} represent the real and imagine part of q_1 respectively.

To recover the quaternion given the 3-D Euclidean representation $\zeta(q_2)$, an exponential operation is conducted.

$$q_2 = \exp(\zeta(q_2)) * q_0 \quad (4)$$

where

$$\exp(\zeta) = \begin{cases} \cos(\|\zeta\|) + \sin(\|\zeta\|) \frac{\zeta}{\|\zeta\|} & \text{if } \zeta \neq 0 \\ 1 + [0 \ 0 \ 0]^T & \text{if } otherwise. \end{cases} \quad (5)$$

2.7. NTT algorithm architecture

The present study utilizes a Convolutional Neural Network (CNN) model for processing input images. The CNN architecture chosen for this purpose consists of five convolutional blocks, each employing a varying number of filters: 8, 16, 32, 64, and 128. Each block comprises two convolutional layers that employ Rectified Linear Unit (ReLU) activation function. Following

the convolutional layers, a max pooling layer is employed to downsample the feature map. As a result, the final feature map dimensions are $128 \times 4 \times 4$. To facilitate further processing, a fully connected layer with 417 neurons, activated by ReLU, is incorporated. The output layer of the model consists of two fully connected layers with linear activation, which yield predictions for both needle position and orientation. A visual representation of the model architecture can be seen in Figure 5.

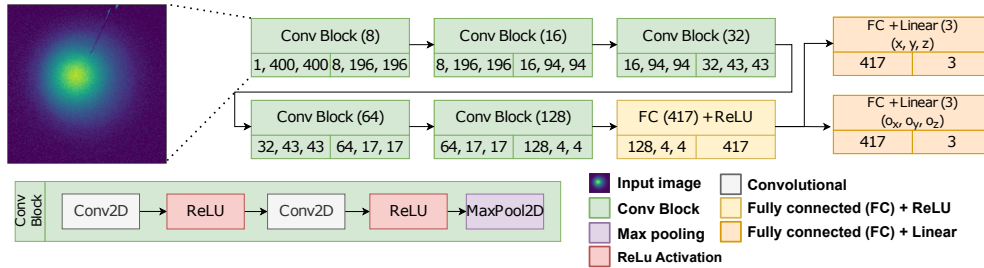


Figure 5: The CNN Architecture for Needle Tip position & orientation estimation with optical imaging as input.

3. Experiments

Two experiments were designed to evaluate the proposed NTT system and algorithm. The first experiment was based on a rubber phantom which is made of homogeneous material. Specifically, we were dedicated to test and compare the system performances with different exposure times. Furthermore, the second experiment was carried out on a more realistic porcine phantom. By employing this sequential approach, the experimental design aims to validate the proposed method in guiding needle insertion during the femoral artery intravenous task. Also, we aims to evaluate the proposed method’s potential in other medical applications that involve more intricate anatomical structures.

The evaluation metrics include positional accuracy, orientation accuracy and processing time. The orientation accuracy is quantified by the absolute value $||\zeta||$ using Equation 3 with q_0 as the ground-truth value and q_1 as the predicted value.

3.1. Preliminary experiment on rubber phantom

The first experiment was conducted on a TruIV block phantom (Limbs & Things Co., UK), which is made of homogeneous rubbery material (Fig-

ure 6(A)). During the experiment, the optic needle was manually inserted into the phantom in various depths and orientations for generating datasets. Specifically, the data were collected within a box with a length of 60 mm, a width of 40 mm and a depth of 45 mm. The insertion angle was kept with the needle bevel tip facing up towards the camera. The pitch ϕ was between 30° and 70° with a yaw θ from -45° to 45° . The data collection process was conducted with even sampling across the defined space.

In total, two datasets were generated, comprising images and the corresponding spatial position of the needle tip in 6-DOFs. One dataset was captured with an exposure time of 20 ms, while the other dataset utilized an exposure time of 100 ms with 511 samples each.

The dataset was divided into three subsets using a 60/20/20 split, where 60% of the data was allocated for training, 20% for validation, and the remaining 20% for testing.

3.2. System evaluation based on porcine phantom

The second set of experiments involved the use of porcine tissue phantoms to create a realistic evaluation environment. For this purpose, two types of phantoms were obtained from the market: a piece of bacon and a piece of fresh pork slab. The size of both phantoms were big enough for ensuring coverage of the camera’s field of view. The bacon phantom featured a 2 mm thick layer of skin and a substantial layer of fat, closely simulating the actual anatomical characteristics of the human groin area. The total thickness of the bacon phantom was measured to be 34.9 ± 2.2 mm. As for the fresh pork phantom, a more complicated anatomic structure was observed with intersecting layers of fat and muscle beneath the skin surface. The overall thickness of the fresh pork phantom was found to be 47.8 ± 3.2 mm. This complex anatomical structure allows us to assess the capabilities of the proposed technology in handling more intricate medical applications.

During the experiment, one of the phantom was placed on the platform, and then, the camera height was adjusted to maintain a distance of 100 mm above the tissue surface. Following this setup, a data collection procedure similar to the one employed in the first experiment was conducted, but only 100 ms exposure time was used. This was because a far better performance was received from the experiments on the rubber phantom (please refer to Section 4.1). During the data collection, the needle was manually inserted into the tissue at various depths and angles, encompassing a range identical to that of the first experiment. Care was taken to ensure a straight needle

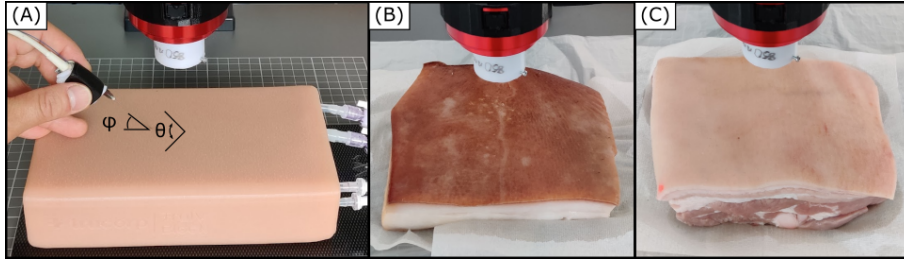


Figure 6: The proposed system was evaluated on (A) a rubber phantom (TruIV block), (B) a bacon phantom, and (C) a fresh pork phantom. The range of needle insertion angle θ and ϕ are illustrated in (A).

shaft before proceeding with data recording, including both the scattering image Img_{res} and the corresponding needle tip position.

In the second experiment, a dataset of 1367 samples on bacon and 1142 samples on fresh was created. The data processing was the same as in the first experiment. The data were divided into a 60/20/20 split for the training, validation and test dataset. The collected data from the second experiment were utilized to train the proposed CNN-based model. The previously identified hyperparameters found effective for the phantom model were applied in this training process.

3.3. Model training and hyperparameter tuning

In order to determine the optimal parameters for the model’s architecture and training, a Bayesian hyperparameter tuning approach was employed with the training and validation split from the rubber phantom. The ranges of the explored parameter values can be found in Table 1. During the model’s training process, a learning rate scheduler was employed if the hyperparameter was true. This scheduler would reduce the current learning rate with a factor of 0.1 if the validation loss of the model did not demonstrate improvement within a span of 30 epochs and terminates the training if no improvement is seen within 100 epochs. The loss function used for the model training is a Mean Squared Error (MSE) loss with the position and orientation $Loss = MSE_p(p, \hat{p}) + \alpha \cdot MSE_o(o, \hat{o})$ where p and o is the ground-truth position and orientation vectors $p = [x \ y \ z]$, $o = [o_x \ o_y \ o_z]$, \hat{p} and \hat{o} the model prediction for the position and orientation and α being the loss weight for the orientation. The Bayesian hyperparameter tuning used the best validation loss score for the parameter search.

Table 1: Parameter ranges for hyperparameter tuning

| Parameter | Range | |
|----------------------------|------------------|------|
| Optimizer | Adam, AdamW, SGD | |
| Batch Size | 4 | 64 |
| Conv Blocks (CB) | 1 | 5 |
| CB initial filter | 4 | 16 |
| Fully Connected layers | 1 | 4 |
| Fully Connected Layer Size | 10 | 512 |
| Use learning rate schedule | Yes | No |
| Loss weight orientation | 0.0, | 1.0 |
| Learning Rate | 1e-9 | 1e-1 |

The following parameter settings were selected from 668 runs: the AdamW optimizer, with a batch size 32. The initial filter count for the convolutional blocks was set to 8 with 5 blocks, while the fully connected layer had a size of 517 neurons with one layer. The learning rate was set to 0.00013 with a learning rate scheduler. The orientation component of the loss was weight with 1.174.

4. Results

4.1. Results based on the rubber phantom

Table 2 presents the computed position accuracy in the X, Y, and Z components, as well as the $L2$ norm, based on the test set. For each component, the mean error, standard deviation (STD) and 90 percentile (90%ile) are reported. To mitigate the influence of random weight initialization, the models were trained independently ten times, and the aggregated results were considered for analysis.

The results in Table 2 indicate that small differences of the position accuracy in the X, Y, and Z component. Additionally, results using 100 ms exposure time are found considerably better compared to the results using 20 ms exposure time.

Moreover, the $L2$ norm errors in different insertion depths Z^* are plotted in Figure 7. The insertion depth Z^* is obtained by subtracting the needle tip’s Z value, relative to the global coordinate, from the height of the phantom. Relatively higher errors are observed from the first 5 mm of depth, while

Table 2: The mean error (*mean*), standard deviation (*STD*) and 90 percentile (*90%ile*) in mm comparing the CNN output and ground-truth on the rubber phantom with 20 and 100 ms exposure time based on the test set.

| Exposure | mean | | STD | | 90th %ile | |
|----------|------|-----|-----|-----|-----------|-----|
| | 20 | 100 | 20 | 100 | 20 | 100 |
| X | 1.7 | 1.1 | 2.6 | 1.0 | 3.5 | 2.7 |
| Y | 3.5 | 1.2 | 2.8 | 1.3 | 7.4 | 2.3 |
| Z | 1.5 | 1.1 | 1.9 | 1.0 | 3.2 | 2.4 |
| L2 | 4.7 | 2.3 | 3.6 | 1.5 | 9.1 | 3.9 |

Table 3: The orientation error obtained from the rubber phantom experiment.

| Exposure | mean | | STD | | 90th %ile | |
|-------------|------|------|------|------|-----------|-----|
| | 20 | 100 | 20 | 100 | 20 | 100 |
| $ \zeta $ | 0.24 | 0.20 | 0.14 | 0.11 | 0.5 | 0.4 |

the results from 5 to 40 mm are found relatively consistent. Also, higher positional accuracy of the system with 100 ms exposure time is found compared to that with 20 ms exposure time.

The orientation accuracy, presented as $||\zeta||$, are presented in table 3. Results of different exposure time, namely 20 ms and 100 ms, are shown together for comparison.

4.2. Results based on porcine phantoms

The positional tracking error based on the bacon and fresh porcine phantoms are summarized in Table 4. Specifically, the errors in the X, Y, and Z directions, as well as their corresponding $L2$ norm are presented. The observed errors in the X, Y, and Z component exhibits similarities: approximately 1.0 mm for the bacon phantom and 1.6 mm for the fresh pork phantom. In fact, the tracking accuracy ($L2$ norm) is higher for the bacon phantom compared to the fresh pork phantom, with values of 2.0 ± 1.2 mm and 3.2 ± 3.1 mm respectively.

The $L2$ norm accuracy in different insertion depths Z^* are shown in Figure 8. The errors observed in the results obtained from the bacon phantom are relatively smaller when compared to those from the fresh pork phantom. This is coherent to the results reported in Table 4. In addition, the results collected from the bacon phantom demonstrate consistency across different insertion depths. In contrast, an increasing trend is evident in the results acquired

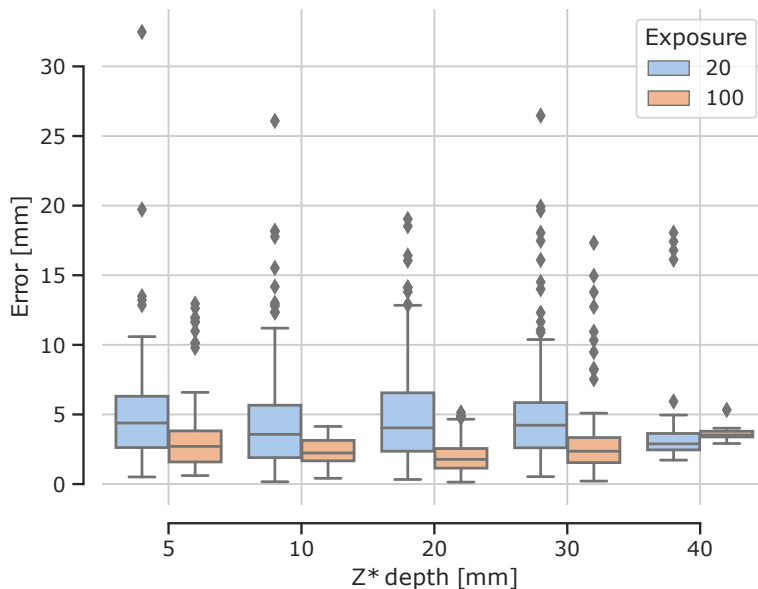


Figure 7: Boxplot of the $L2$ norm error against different depths inside the rubber phantom Z^* .

from the fresh pork phantom. In addition, the needle tip orientation tracking errors are provided in Table 5. Slightly higher accuracy in tip orientation estimation is found on the bacon phantom (0.16 ± 0.1 rad) compared to the fresh pork phantom (0.19 ± 0.1 rad).

4.3. Processing time

The proposed system and the CNN based tracking algorithm was implemented and tested on a portable PC, NUC (Intel i7 CPU). In addition to the camera's frame rate, the processing time was found to be 20.2 ± 0.8 ms. Notably, the processing time can be further reduced to sub-millisecond when the same algorithm was tested on a computer with GPU. This observation suggests that the proposed system is sufficiently fast for real-time tracking of the needle tip, even when implemented on a portable setup.

5. Discussion

Through a comparison of the results obtained from the rubber phantom, it is evident that the positional error with a 20 ms exposure time (4.7 ± 3.6 mm)

Table 4: The mean error (*mean*), standard deviation (*STD*) and 90 percentile (*90%ile*) in mm comparing the CNN output and ground-truth on both the bacon phantom (*Bacon*) and the fresh pork phantom (*Fresh*) based on the test set.

| Phantom | mean | | STD | | 90th %ile | |
|---------|-------|-------|-------|-------|-----------|-------|
| | Bacon | Fresh | Bacon | Fresh | Bacon | Fresh |
| X | 0.9 | 1.5 | 0.8 | 2.0 | 2.0 | 3.1 |
| Y | 1.0 | 1.6 | 0.8 | 2.4 | 2.0 | 3.2 |
| Z | 1.2 | 1.6 | 1.0 | 1.4 | 2.5 | 3.4 |
| L2 | 2.0 | 3.2 | 1.2 | 3.1 | 3.6 | 5.4 |

Table 5: Orientation error of needle tip tracking results on the bacon phantom (*Bacon*) and the fresh pork phantom (*Fresh*).

| Phantom | mean | | STD | | 90th %ile | |
|-------------|-------|-------|-------|-------|-----------|-------|
| | Bacon | Fresh | Bacon | Fresh | Bacon | Fresh |
| $ \zeta $ | 0.16 | 0.19 | 0.10 | 0.10 | 0.3 | 0.3 |

is higher than that with a 100 ms exposure time (2.3 ± 1.5 mm). These findings highlight the significance of exposure time as a key factor in generating adequate intensity on the tissue surface, particularly when the needle is inserted to depths of up to 40 mm. Nevertheless, an alternative approach to enhance lighting intensity can be through increasing the power of the light source, a factor that will certainly be optimized in our future study.

Based on the results obtained from the porcine experiment, the $L2$ norm errors derived from the bacon phantom remained within 3.6 mm, whereas the errors from the fresh pork phantom are generally higher, mostly within 5.4 mm. In fact, the bacon phantom more closely resembles the anatomy of the human groin area, where mostly consists of fat. Therefore, the achievement of a 3.6 mm error demonstrates the efficacy of the proposed technology, considering that the radius of the femoral artery typically ranges from 4 to 5 mm. Also, the proposed method is considered sufficient for this application since only the tracking accuracy in X and Y direction are more critical to target the needle to the artery.

The results obtained from the fresh pork phantom exhibit reasonable performance up to an insertion depth of 30 mm. However, the errors noticeably escalate from $Z^* = 30$ mm to 40 mm, as shown in Figure 8. This occurrence can be attributed to the significant reduction in light intensity captured by

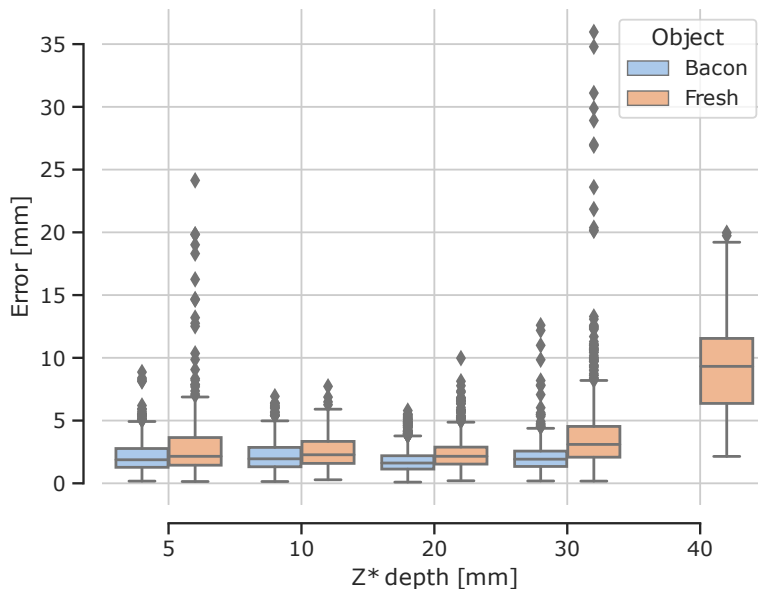


Figure 8: Boxplot of the L_2 norm error against different insertion depths Z^* on the bacon phantom (*Bacon*) and the fresh pork phantom (*Fresh*).

the camera. In Figure 9, examples of imaging from two different depths (10 mm and 30 mm) for both the bacon and fresh pork phantoms are provided. It is evident that the lighting intensity for the fresh pork phantom at $Z^* = 30\text{ mm}$ becomes hard to discern, whereas the lighting from the needle tip at the same depth remains distinguishable for the bacon phantom. This can be interpreted due to the higher concentration of muscle in the fresh pork phantom, which absorbs a greater amount of light (near-infrared in this study), affecting the intensity of the captured images. Given the tracking error within 5.4 mm, the proposed system is still demonstrated to be able for easy extension to various medical applications with more complex anatomical features.

Furthermore, we can see that a slightly higher error is observed for $Z^* \leq 5\text{ mm}$ in the results obtained from the rubber phantom (Figure 7). This discrepancy is suspected to be caused by the insufficient number of samples collected near the surface of the phantom. To avoid this, an additional 100 samples were collected from the near-surface $Z^* \leq 10\text{ mm}$ during the experiments conducted on the bacon and the fresh pork phantoms. Consequently, it is found that the error in the near-surface area is not higher than that in the subsurface region, as shown in Figure 8.

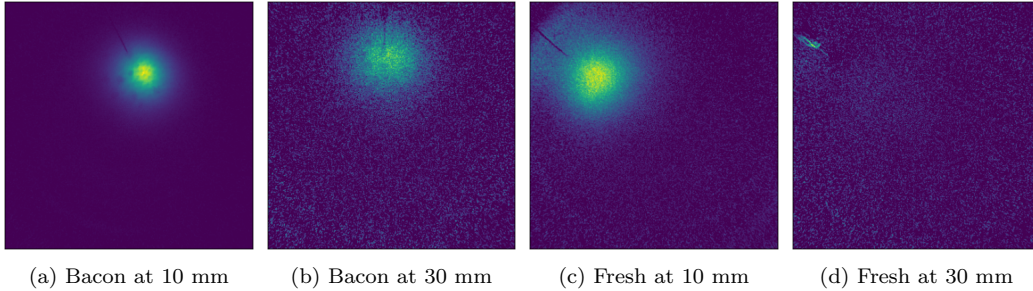


Figure 9: Examples of optical imaging with the bacon phantom (*Bacon*) and the fresh pork phantom (*Fresh*) at two insertion depths 10 and 30 mm.

It is also interesting to see that the darkened skin of the bacon phantom surprisingly does not excessively hinder the passage of light. As a result, the camera is still able to capture high-intensity images even at greater insertion depths. This finding is encouraging as it suggests that the system possesses robust potential for use across different skin tones. Our future study will explore the incorporation of skin tone as an input to the AI model, with the goal of enhancing the model’s generalization capabilities.

In this study, the accuracy of needle orientation tracking is measured by the $||\zeta||$ value, which ranges from 0 to π , with smaller values indicating higher accuracy. The results of this study demonstrate that the orientation accuracy achieved is commendable. While it may not be critical for this specific application, the ability to track needle orientation holds significant importance in other medical applications, such as needle steering.

Lastly, this study has a few limitations that should be acknowledged. Firstly, the power of the light source has not been optimized in this study. For safety considerations, an ultra-low power light source (0.6 mW) is chosen. However, it is possible to utilize a relatively higher power light source. In this case, it would be feasible to reduce the exposure time of the camera while maintaining a comparable level of imaging quality. Secondly, despite our efforts to ensure a straight needle shaft during data collection, small manual errors may still involve, affecting the consistency of the transformation matrix between the needle tip and the EM sensor. While these errors are challenging to completely eliminate, multiple measures were taken to minimize their impact. Additionally, the above positional accuracy in each case must be assessed in relation to the system’s calibration. Namely, the Euclidean distance reprojection error, 0.64 mm, should be taken into account

when evaluating the system’s performance. Also, to use this method in practise, extended reality technique can be integrated in the future for guiding the whole insertion process [20].

6. Conclusion

This study presents a cutting-edge technology aiming to achieve precise and efficient needle tip tracking during the insertion to a deep subsurface location. The system is developed through combining optical imaging and AI-based algorithms. Experimental evaluations conducted on rubber and porcine tissue phantoms validate the system’s capability for accurate and real-time tracking of the needle tip during the insertion procedure. In addition, the results highlight the potential of the system to enhance the safety and efficiency of femoral artery insertion procedures, and demonstrate its versatility for different medical applications.

Acknowledgement

We would like to thank Andrea Blasi Núñez, Yeongjun Hong and Beatriz Moreira Santos for their technical supports. This study is supported by the Innovation Fund Denmark under the agreement 1061-00071A.

References

- [1] G. McLeod, Novel approaches to needle tracking and visualisation, *Anaesthesia* 76 (2021) 160–170.
- [2] P. Beigi, S. E. Salcudean, G. C. Ng, R. Rohling, Enhancement of needle visualization and localization in ultrasound, *International journal of computer assisted radiology and surgery* 16 (2021) 169–178.
- [3] M. G. Wagner, S. Periyasamy, M. A. Speidel, P. F. Laeseke, Feasibility of 3d motion-compensated needle guidance for tips procedures, in: *Medical Imaging 2020: Image-Guided Procedures, Robotic Interventions, and Modeling*, Vol. 11315, SPIE, 2020, pp. 30–36.
- [4] J. Pan, D. Yu, R. Li, X. Huang, X. Wang, W. Zheng, B. Zhu, X. Liu, Multi-modality guidance based surgical navigation for percutaneous endoscopic transforaminal discectomy, *Computer Methods and Programs in Biomedicine* 212 (2021) 106460.

- [5] M. Engberg, S. Mikkelsen, T. Hörer, H. Lindgren, E. Søvik, M. Frendø, M. B. Svendsen, L. Lönn, L. Konge, L. Russell, et al., Learning insertion of a resuscitative endovascular balloon occlusion of the aorta (reboa) catheter: Is clinical experience necessary? a prospective trial, *Injury* 54 (5) (2023) 1321–1329.
- [6] M. Koskinopoulou, Z. Cheng, A. Acemoglu, D. G. Caldwell, L. S. Mattos, Robotic devices for assisted and autonomous intravenous access, *IEEE Transactions on Medical Robotics and Bionics* (2023).
- [7] B. Konh, B. Padasdao, Z. Batsaikhan, S. Y. Ko, Integrating robot-assisted ultrasound tracking and 3d needle shape prediction for real-time tracking of the needle tip in needle steering procedures, *The International Journal of Medical Robotics and Computer Assisted Surgery* 17 (4) (2021) e2272.
- [8] L. J. Brattain, T. T. Pierce, L. A. Gjestebj, M. R. Johnson, N. D. DeLosa, J. S. Werblin, J. F. Gupta, A. Ozturk, X. Wang, Q. Li, et al., Ai-enabled, ultrasound-guided handheld robotic device for femoral vascular access, *Biosensors* 11 (12) (2021) 522.
- [9] Z. Cheng, B. L. Davies, D. G. Caldwell, L. S. Mattos, A hand-held robot for precise and safe pivc, *IEEE Robotics and Automation Letters* 4 (2) (2019) 655–661.
- [10] Z. Cheng, A. L. C. Carobbio, L. Soggiu, M. Migliorini, L. Guastini, F. Mora, M. Fragale, A. Ascoli, S. Africano, D. G. Caldwell, et al., Smartprobe: a bioimpedance sensing system for head and neck cancer tissue detection, *Physiological measurement* 41 (5) (2020) 054003.
- [11] J. C. Romero, T. M. Peters, E. C. Chen, Development of a mini stereotactic guidance system for percutaneous focal liver tumor ablation, in: *Medical Imaging 2022: Image-Guided Procedures, Robotic Interventions, and Modeling*, Vol. 12034, SPIE, 2022, pp. 568–576.
- [12] A. M. Franz, T. Haidegger, W. Birkfellner, K. Cleary, T. M. Peters, L. Maier-Hein, Electromagnetic tracking in medicine—a review of technology, validation, and applications, *IEEE transactions on medical imaging* 33 (8) (2014) 1702–1725.

- [13] P. Moreira, K. J. Boskma, S. Misra, Towards mri-guided flexible needle steering using fiber bragg grating-based tip tracking, in: 2017 IEEE International Conference on Robotics and Automation (ICRA), IEEE, 2017, pp. 4849–4854.
- [14] E. Durand, M. Penso, T. Hemery, T. Levesque, G. Moles, C. Tron, N. Bouhzam, N. Bettinger, S. Wong, J.-N. Dacher, et al., Standardized measurement of femoral artery depth by computed tomography to predict vascular complications after transcatheter aortic valve implantation, *The American Journal of Cardiology* 145 (2021) 119–127.
- [15] How deep is the femoral artery?, accessed: 2023-07-03.
URL <https://www.healthtap.com/questions/1151063\how-deep-is-the-femoral-artery/>
- [16] D. A. Boas, C. Pitris, N. Ramanujam, *Handbook of biomedical optics*, CRC press, 2016.
- [17] A. Paszke, S. Gross, F. Massa, A. Lerer, J. Bradbury, G. Chanan, T. Killeen, Z. Lin, N. Gimeshein, L. Antiga, A. Desmaison, A. Kopf, E. Yang, Z. DeVito, M. Raison, A. Tejani, S. Chilamkurthy, B. Steiner, L. Fang, J. Bai, S. Chintala, PyTorch: An Imperative Style, High-Performance Deep Learning Library, in: H. Wallach, H. Larochelle, A. Beygelzimer, F. d’Alché Buc, E. Fox, R. Garnett (Eds.), *Advances in Neural Information Processing Systems* 32, Curran Associates, Inc., 2019, pp. 8024–8035.
URL <http://papers.neurips.cc/paper/9015-pytorch-an-imperative\style-high-performance-deep-learning-library.pdf>
- [18] W. Falcon, The PyTorch Lightning team, PyTorch Lightning (Mar. 2019). doi:10.5281/zenodo.3828935.
URL <https://github.com/Lightning-AI/lightning>
- [19] Y. Huang, F. J. Abu-Dakka, J. Silvério, D. G. Caldwell, Generalized orientation learning in robot task space, in: 2019 International Conference on Robotics and Automation (ICRA), IEEE, 2019, pp. 2531–2537.
- [20] R. Moreta-Martínez, I. Rubio-Pérez, M. García-Sevilla, L. García-Elcano, J. Pascau, Evaluation of optical tracking and augmented reality

for needle navigation in sacral nerve stimulation, *Computer Methods and Programs in Biomedicine* 224 (2022) 106991.